Spectrochimica Acta Part B: Atomic Spectroscopy 241 (2026) 107537

Contents lists available at ScienceDirect

Spectrochimica Acta Part B: Atomic Spectroscopy

journal homepage: www.elsevier.com/locate/sab

Plasma–atmosphere interactions and implications for the characterization of carbon-bearing samples with LIBS on Mars

E. Clavé [a,b,*], K. Rammelkamp [a], F. Seel [a], P. Hansen [a], C.H. Egerland [a], S. Schröder [a]

[a] DLR Institute for Space Research, Rutherfordstr. 2, Berlin, 12489, Germany
[b] Université Claude Bernard Lyon 1, ENS de Lyon, CNRS, UJM, LGL-TPE, UMR 5276, Villeurbanne cedex, F-69622, France

ARTICLE INFO

Keywords:
LIBS
Mars
Carbon
Carbonate

ABSTRACT

Carbon is a key element on Mars, where it is present in the atmosphere, cryosphere and rocks. It has influenced the Martian climate over billions of years, and records the conditions of past habitable environments. Laser-Induced Breakdown Spectroscopy (LIBS) is an efficient technique for fast in situ analysis of the chemical composition of rocks on the Martian surface, used on several Mars exploration missions already. However, to characterize the carbon content of rocks with LIBS on Mars, one must take into account the contribution of the CO_2-dominated Martian atmosphere to the signal recorded in LIBS spectra. In support of LIBS analyses on Mars, we investigate this atmospheric contribution using a plasma-imaging setup in the laboratory. We study the temporal and spatial dynamics of the carbon and oxygen signals in different experimental configurations, where these elements originate from either the sample or the atmosphere. The significance of the atmospheric contribution to the carbon and oxygen signal in Martian atmospheric conditions is highlighted. We show that C I emissions come from different areas of the plasma depending on the origin of the carbon; such difference is not observed in the spatial distributions of C II, O I or O II. The C II / C I ratios are different in atmospheric and sample contributions, with a higher relative abundance of C I in the atmospheric contribution. To recognize carbonate in Martian LIBS data, we recommend using C I / O I if possible, or C II / O I ratios, with appropriate precautions.

1. Introduction

Martian carbon – stakes, carbonates. Carbon is a key element on Mars, where it is present in the atmosphere, the cryosphere and the rocks. It has influenced the Martian climate over billions of years, and records the conditions of past habitable environments on the red planet. The characterization of carbon on the surface of Mars, in mineral or organic form, is therefore of particular interest for in situ missions. Martian carbonates, in particular, have been researched and discussed for decades [1,2] and keep providing new constraints on the past Martian climate [3,4].

Few analytical techniques enable the detection, let alone quantification, of carbon in rocks in situ, and even fewer can do it remotely with only short acquisition times and with no sample preparation. Carbonate minerals have so far been detected in situ in Martian rock or soil targets with Mössbauer (MB) [5], near-infrared reflectance (NIR) [6,7], X-ray diffraction (XRD) [3], Raman spectroscopy [8,9] and Laser-induced Breakdown Spectroscopy (LIBS) [4,8]; carbonates have also been inferred with X-ray Fluorescence (XRF) [10,11]. These carbonate detections mostly rely on the characterization of the mineralogy (eg. vibrational techniques), since most techniques which measure the elemental composition, with the exception of LIBS, are not sensitive to low-Z elements and thus cannot detect carbon directly (eg. XRF). Organic carbon has been detected with Evolved Gas Analyzer (EGA), gas chromatograph-mass spectrometer and combustion experiment from the SAM instrument [12–14], as well as Raman spectroscopy [15,16]. LIBS is therefore the only technique performing in situ analysis on Mars with the potential to quantify carbon, remotely as well as under an hour [17,18].

LIBS on Mars. The use of LIBS (Laser-induced Breakdown Spectroscopy) for in situ analysis on the surface of Mars has been investigated for many years [19–21], and successfully implemented since 2012 with the ChemCam instrument onboard NASA's Curiosity rover [22,23], followed by the MarsCode instrument onboard the Chinese Zhurong rover [24] and the SuperCam instrument onboard NASA's Perseverance rover [25,26]. Using these three instruments, the chemistry of thousands of rocks was characterized by analyzing the

* Corresponding author at: Université Claude Bernard Lyon 1, ENS de Lyon, CNRS, UJM, LGL-TPE, UMR 5276, Villeurbanne cedex, F-69622, France.
E-mail address: elise.clave@univ-lyon1.fr (E. Clavé).

https://doi.org/10.1016/j.sab.2026.107537
Received 24 February 2026; Received in revised form 4 April 2026; Accepted 20 April 2026
Available online 22 April 2026

line emissions of a plasma induced by laser ablation on the targets of interest. Appropriate models enable to derive quantitative chemical composition of the targets from the LIBS data, especially for the major elements [27,28]. Typically quantified oxides are SiO_2, TiO_2, Al_2O_3, FeO, MgO, CaO, Na_2O and K_2O; other measured elements include Li, B, Cr, V, Mn, Ni, Cu, Rb, Sr, Ba, Zn, C, H, N, O, P, F, Cl, with variable limits of detections [26,29].

Challenge of characterizing carbon with LIBS on Mars. One of the challenges of the interpretation of LIBS data is to differentiate signal coming from the sample or from the atmosphere. In particular, every LIBS spectrum measured in the Martian atmosphere, which is composed of 96% CO_2 [30], shows carbon and oxygen emission lines. This is due to the breakdown of atmospheric CO_2 molecules through interaction with the plasma [31–33].

The emission lines typically used to characterize carbon and oxygen signal in LIBS in Martian atmosphere are C III 230 nm, C I 247.9 nm, C II 658.1 nm, C II 678.5 nm, C II 723.3 and 723.8 nm for carbon, and O II 441.6 nm and O I 777.5 nm for oxygen [8,32–40]. Further line selection depends on the context (laboratory vs. in situ), the characteristics of the spectrometer, the application and the composition of the considered targets (e.g. Fe interferences with C I 248 nm).

An often used strategy to account for atmospheric contribution to the carbon signal in Martian LIBS consists in normalizing the carbon signal to the oxygen signal [31,32]. An important constraint for this approach is that only lines of similar ionization degree should be ratioed together, to avoid the influence of different laser radiances, decay times, etc. [33,41]. Unfortunately, this is not necessarily applicable to the analysis of in situ LIBS data acquired with ChemCam or SuperCam on Mars, where often only C II (658 nm, 678 nm, 723 nm) and O I (777 nm) lines are usable [8,39], due in part to the interference of Fe emissions. Parameters like laser irradiance, and thus distance to the target, do not affect lines of different ionization degrees in the same way, and precautions thus have to be taken to correct for their influence on the C / O values if lines of different ionization degrees (eg. C II and O I) are used [4,8,39].

The characterization of carbon with LIBS in Martian atmospheric conditions thus requires further work, to understand the interactions between the plasma and the atmosphere and the characteristics of the atmospheric contribution to the LIBS signal.

Plasma imaging. Although plasma emissions are generally integrated spatially with space instruments to measure in-situ LIBS spectra, plasma imaging is an experimental approach which enables to look at the spatial heterogeneity of the plasma and investigate the dynamics of the plasma expansion and its interactions with the atmosphere. It has been used previously with slightly different approaches to study the spatial distribution of species or variability of plasma parameters within the plasma [38,42–44] or observe the expansion of the plasma in different atmospheric conditions including those of Earth and Mars [45]. It has also been used to investigate the contribution of the atmosphere to the LIBS signal [46], highlighting the complex mixing of species originating from the sample or the ambient medium inside the plasma. This shows the potential of plasma imaging to study more deeply the interactions of the plasma and the atmosphere.

This study. To investigate LIBS plasma–atmosphere interactions for improved in-situ analysis of carbon-bearing samples on Mars, we present temporally and spatially resolved LIBS data measured in the laboratory in different atmospheric conditions. Measurements were done on carbon-bearing and carbon-free samples as well as in atmospheric conditions with and without CO_2 to isolate the contributions of the sample and atmosphere to the carbon signal, respectively. From this data, we derive and discuss implications for identification of carbon-bearing samples with LIBS on Mars.

2. Method

2.1. Experimental setup

The plasma imaging setup used for this study was described in details in previous studies [38,45] and is illustrated in Fig. 1. It relies on a 1064 nm Nd:YAG laser (Quantel Viron) delivering 8.1 ns pulses of about 11.9 ± 0.8 mJ to an area of ~900 μm^2 on the sample surface. Samples are placed in an air-tight simulation chamber for control of the composition and pressure of the ambient gas. The light of the plasma is imaged on the detector of a Czerny Turner spectrometer (Andor Solis) equipped with an intensified CCD. The image of the plasma on the detector is rotated by 90°, with the horizontal extent of the plasma being imaged in each column, parallel to the entrance slit, and the height of the plasma along the rows. In the setup, the vertical imaging position is adjustable, to accommodate samples of different thicknesses, and cover different parts of the plasma plume.

Two different acquisition modes of the spectrometer are used. To acquire time-resolved spectra (called TR data in the following), the opening of the entrance slit is set to 100 μm and the setup is used in *Full Vertical Binning* (FVB) mode, i.e. summing all the pixels of a given column on the detector. With such a narrowly-opened slit, the emission of only a thin horizontal section of the plasma is collected, and imaged onto a few columns of the CCD. In this mode, the spatial information is lost, but the spectral resolution and signal to noise ratio (SNR) are improved. To image the plasma, the *Imaging* mode with a fully open entrance slit (2500 μm) is used, providing the plasma images (called PI). Using the appropriate grating within the spectrometer, the spectral range of interest can be selected. Then, the vertical extent of the plasma and the spectral information are convoluted on the same axis of the images. Recording PIs of specific elemental emission lines therefore requires the lines to be sufficiently isolated (> 2–3 nm each side with the 240 nm blaze grating; > 10 nm with the 750 nm blaze grating, typically). Additionally, plasma height might be overestimated in the images if the diffraction of the grating is not taken into account. To image the O I 777 nm signal, a bandpass filter centered at 780 nm with a FWHM of 10 nm (Edmund Optics) is added to the optical path, as illustrated in Fig. 1.

The simulation chamber is pressurized and hermetically sealed; the pressure is maintained between 6 and 7 mbar to match Mars surface conditions. Either air or Mars simulant gas (96% CO_2, traces of Ar and N_2, Linde) is used both at the same pressure to ensure consistent plasma confinement conditions. We refer to the Mars simulant gas as CO_2 in the rest of this study.

2.2. Samples

The suite of samples was chosen with the simplest possible compositions to minimize overlap of lines with the carbon and oxygen lines of interest and to be relevant to the Mg-rich carbonates detected in Jezero Crater [4,8,9]. For comparable laser-target coupling between samples, we used only pressed pellets. Three pure pellets were prepared (1 g of reagent grade powders pressed for 10 min under a pressure of 5 tons): graphite, Mg-carbonate, Mg-sulfate. The Mg-carbonate is anhydrous. For the Mg-sulfate, we started with an anhydrous Mg-sulfate powder, to reduce the influence of H, which had the dual advantage of (i) limiting interference with the 658 nm line of C II and (ii) keeping the sample composition as simple as possible to maximize comparability of the different samples and configurations. However, the pellet was unstable, absorbing water, resulting in an unreliable understanding of the actual water content of the sample. We thus switched to a $MgSO_4 \times 1 H_2O$ powder, with finer grains, more similar to the other powders used in this study, and much more stable than its anhydrous equivalent. An image of the pellets is included in Supplementary Material (Figure S1).

To observe the dynamics of C and O in the laser-induced plasma depending on their origin, we combine atmospheric and sample compositions in four experimental configurations, summarized in Table 1.

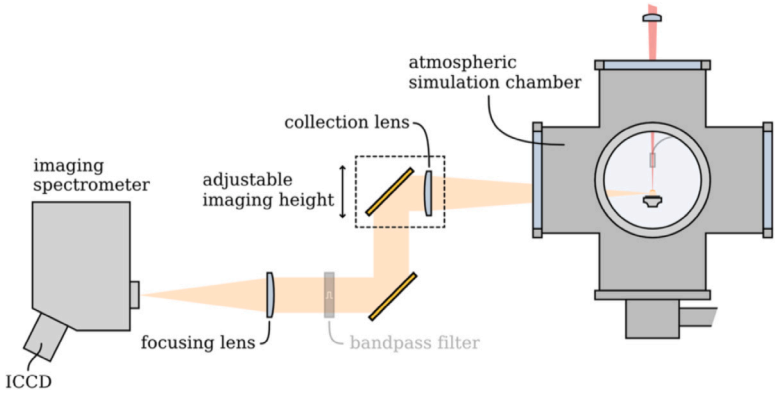

Fig. 1. Plasma imaging setup. The sample is placed in the atmospheric simulation chamber, for control of the ambient conditions. The plasma is generated by focusing the pulsed laser along the vertical axis on the surface of the sample. The emission of the plasma is collected with a lens, located to the side and focused on the entrance slit of the imaging spectrometer. The imaging height can be adjusted, and/or a filter inserted between the plasma and spectrometer for selection of the signal to be analyzed.
Source: Copied from [47].

Table 1
Overview of the four experimental configurations: sample and atmospheric conditions. For both air and CO_2, the measurements were done at around 6–7 mbar pressure.

	No C in the atmosphere	C in the atmosphere
No C in the sample	–	Mg-sulfate / CO_2
C in the sample	Mg-carbonate / air Graphite / air	Mg-carbonate / CO_2

Note: Although some carbon is technically present in air, it is denoted as 'no C' in the atmosphere as the amount is negligible.

2.3. Data acquisition

All data are acquired as time series to document the temporal evolution of the signals of interest. Two sets of temporal parameters, initial delay D_0, time step D_{step} and gate width G, are used, with ten steps each, to cover lifetimes of singly ionized and atomic species (same time parameters for TR and PI data): (i) $D_0 = 50$ ns; $G = 50$ ns; $D_{step} = 50$ ns (series called s1); (ii) $D_0 = 100$ ns; $G = 100$ ns; $D_{step} = 300$ ns (series called s2). Series s1 are acquired for all lines while s2 series are only acquired for neutral lines, as they have longer lifetime. For each step of each time series, spectra of 10 laser-induced plasmas are accumulated to increase the signal to noise ratio. All TR data are acquired with a CCD intensifier gain 1000; the gain is set to 2500 for all PI data. In figures, the time indicated for each image corresponds to the center of the acquisition gate ($D + G/2$).

During acquisition, the laser beam is moved over the surface, so that ablation takes place on a pristine surface at all times, leading to similar laser-target interaction and thus repeatable conditions.

Time-resolved LIBS spectra. For each line of interest, TR spectra were first acquired to assess the risk of line interferences and the feasibility of plasma imaging.

Plasma imaging. PI data were then acquired for the lines which are spectrally isolated enough (C I 248 nm, C II 251 nm and O II 689 nm), or for which we have a bandpass filter (O I 777 nm) enabling to remove unwanted emissions. For neutral lines, which last longer and are detected further from the samples' surface, images acquired at two distinct imaging heights are required to cover the whole plasma (Fig. 1). We call H0 the image which covers the sample surface and lower part of the plasma; image H1 is acquired 1.75 mm higher than H0 (same as [45]). H0 and H1 images are then stitched together to produce an image of the entire plasma emission. The horizontal extent of the imaged plasma is determined by the width of the slit, which is a physical constraint of the setup and cannot be changed. For most of the plasmas imaged in this study, this is not a problem as the width of the plasma fits entirely in this field of view; only for O I at delays longer than 1 μs the plasma is possibly larger than what is imaged by the slit, but the signal is very weak at that stage anyways (Figure S5).

A summary of the data acquired in this study in presented in Supplementary Material (Table S1).

2.4. Data processing

Time-resolved LIBS spectra. The only preprocessing step applied to the TR spectra is the subtraction of the dark spectrum which is performed directly in the data acquisition software of the spectrometer.

Plasma imaging. Plasma imaging data require some processing, the different steps are illustrated in Fig. 2 and detailed below. In the following, the images are oriented with the sample at the bottom, the plasma expanding along the vertical axis. The words column and row are used to refer to a vertical or horizontal unit of pixels, respectively. With the plasma imaging a side-view intensity image is recorded, where each pixel's value is the line-of-sight integral of the plasma's radial emission coefficient. This measured intensity profile is mathematically the Abel transform of the true emission distribution [48]. Thus, an Abel inversion is required to obtain the underlying distribution. We will not go into detail about the specific algorithm used here but refer to [38] as we used the python code developed for this study.

1. For each image (H0 and possibly H1, if two imaging heights are used):
    - Subtract dark measurement (performed directly in the data acquisition software).
    - Extract baseline noise level: compute the standard deviation of an area of the original image away from the image of the slit (columns 2 to 180).
    - Set lowest intensity pixels to 0 to reduce the noise.
    - Find the symmetry axis of the image: sum the signal per column of pixels, fit the distribution with a pseudo-Voigt profile; the center of this profile is the symmetry axis of the plasma.
    - Fit a 3D baseline to the image and subtract it. The fit fails for a few 3D baselines, in which case they are not subtracted from the images.
    - Crop region of interest of the image around the plasma (200 pixels each side of symmetry axis horizontally; height: 220 to 290 pixels depending on line considered).

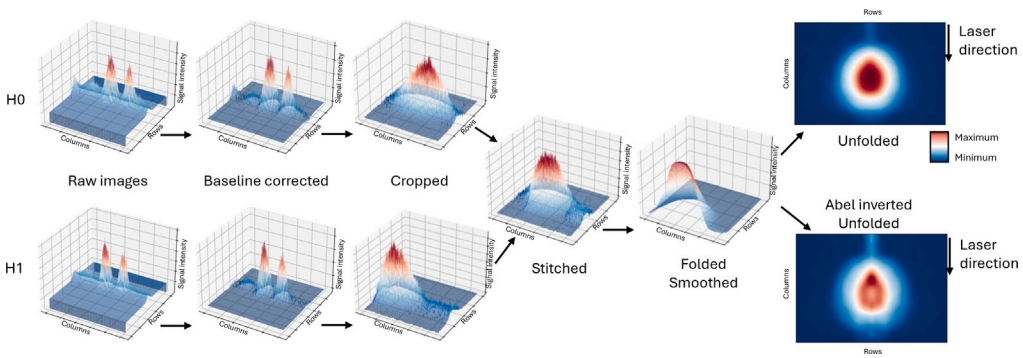

Fig. 2. Illustration of processing pipeline, for an image of C I 248 nm on Mg-carbonate in CO_2, acquired with a gate of 50 ns and a delay of 100 ns. The color range of each image is internal to maximize contrast: blue for the minimal value, white for the half maximum and red for the highest signal. (For interpretation of the references to color in this figure legend, the reader is referred to the web version of this article.)

- Fold image along its symmetry axis (average both sides).

2. Stitch H0 and H1 images together if two imaging heights are used (i.e. for C I 248 nm and O I 777 nm lines).
   - Pixel lines corresponding to same plasma locations in H0 and H1 images were manually identified, to localize the overlapping area.
   - The stitched image is then assembled as follows: the bottom rows of the H0 image are used as is; the overlapping rows of H0 and H1 images are averaged together; the top rows of image H1 are used as is. To make for a smooth image, the top and bottom sections are normalized so that the stitching line matches with the intensity of the averaged section.
3. Smoothing. The Abel inversion step that comes next is very sensitive to noise, hence a strong smoothing and denoising approach.
   - Set highest intensity pixels to their min value.
   - Set lowest intensity pixels to 0.
   - Gaussian filter: sigma = 8.
4. Abel inversion: This step enables to invert the integration of the signal along the line of sight through the plasma, and see the actual internal structure of the emitting species. The Python script developed in [38] is used.
5. Final steps:
   - Unfolding (cutting external 10 and central 2 columns because of border effects).
   - Smoothing: Set lowest intensity pixels to 0.

For smoothing, multiple approaches were considered, including the use of Uniform or Savitzky–Golay filters, as well as denoising using wavelet decomposition, and smoothing before and/or after Abel inversion. The choice of filters and parameters was the least complex one which yielded the apparent best result (denoising with limited apparent loss of information), after testing many combinations and parameters.

Some quantitative characteristics of the signal are also extracted from the plasma imaging data.

- Emission width: in smoothed images (after step 3), the signal is projected onto the horizontal axis (parallel to the surface of the sample), i.e. the signal for each column of the image is summed; the distribution is fitted with a pseudo-Voigt profile (lmfit package, Python) and the width of this profile (full width half maximum, FWHM) is extracted. The width is not calibrated to real life distance units, but the readers are referred to [45] for a precise characterization of plasma sizes in different atmospheric conditions.
- Total signal per image: computed either directly after step 1, when no stitching is applied, or directly after stitching (i.e. before Step 3: Smoothing). Note that for a few images this will include signal from a second line in addition to the line of interest, but at the scale of the time series, this should not be too significant. Images with signal below noise level (extracted before any processing) are to be considered carefully for interpretation; they are represented with low opacity throughout the paper.
- Time-integrated signal: for each line and configuration, the area under the decay curve (signal as a function of time, see Fig. 7) is integrated (using the scipy.integrate package) to derive the time-integrated signal, for comparison with the long-gate spectra acquired with ChemCam and SuperCam on Mars.

TR spectra correspond to the signal coming from a thin cut of the plasma, at fixed height. They are therefore not representative of the whole plasma emissions and are not used to compare signal intensities. Longer delay images (series s2) are used only to extract quantitative parameters; the signal is not of sufficient quality for Abel inversion or to look closely at spatial distributions after 500 ns (Figures S5, S6).

3. Results

3.1. Time-resolved LIBS spectra

Examples of TR spectra from series s1 at one time step (delay 100 ns, gate 50 ns) acquired for the four experimental configurations and the different spectral ranges of interest are presented in Fig. 3. The identification of a few of the emissions lines in these spectra was not clear. For example, some lines visible only with the sulfate sample could correspond to S or a trace element in the reagent powder, but no good match was found in the NIST database based on the line positions and lifetimes.

In these spectra (Fig. 3), the significance of the atmospheric contribution to the LIBS signal is directly observable in the differences between spectra acquired in air (in blue) and in CO_2 (in red/orange).

On the one hand, it appears that the 658 nm, 678 nm and 723 nm C II lines, which are most commonly used for Mars data, are relatively weak and suffer from significant interferences of neighboring lines. For these reasons, these are not usable for PI. On the other hand, the C II doublet around 251 nm and the O II line around 689 nm are strong and isolated enough to be used for plasma imaging, which led to the choice of these lines in this study.

3.2. Plasma imaging

Plasma imaging series for the four lines of interest are shown in Supplementary Material: Figures S3 and S4 (series s1, cropped and smoothed, respectively). Images acquired at the same time (delay) are

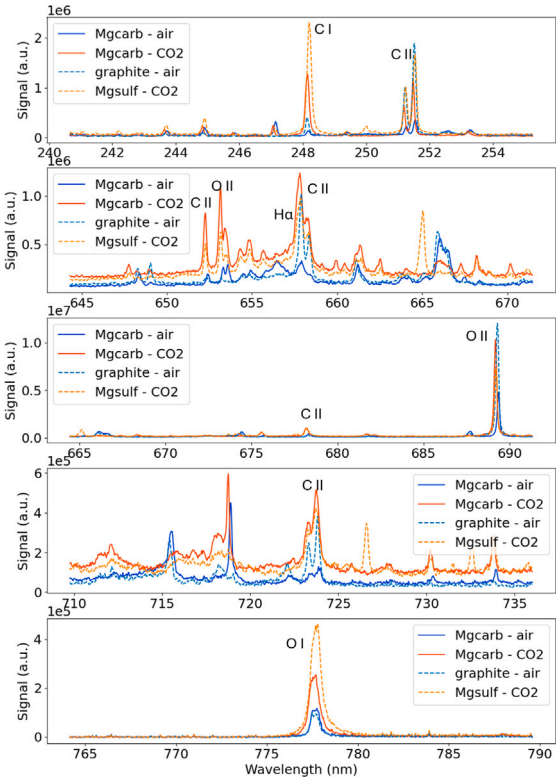

Fig. 3. Examples of spectra in the four experimental configurations, in the 5 spectral ranges of interest, acquired with a delay of 100 ns and a gate of 50 ns. Orange/red for CO_2, blue for air. O I spectrum around 777 nm acquired with bandpass filter (corresponding spectra without the filter are shown in Figure S2). Lines were identified based on peak position and rapidity of signal decay, based on the NIST database [49]. (For interpretation of the references to color in this figure legend, the reader is referred to the web version of this article.)

displayed in the same column, with the delay increasing from left to right in the Figure, showing the temporal evolution of the plasma emissions. The faster decay of ionized lines (C II and O II, bottom of the figures) compared to neutral ones (C I and O I, top of the figures) is clearly visible (Figures S3 and S4).

Spatial distribution of carbon and oxygen signals. Abel inverted image series for the four lines of interest are shown in Figs. 4 and 5 for C and O signals, respectively (series s1).

For both C and O (Figs. 4 and 5), the spatial distribution of neutral lines appears wider (larger apparent plasma) than for ionized lines, for both elements, although it is more significant for oxygen lines.

Focusing on carbon (Fig. 4), in the first image (time 75 ns) in air conditions (top 2 lines), two plasmas are visible. The bottom one corresponds to the carbon line of interest. In the C I images, the top plasma corresponds to the C II 251 nm emission, which then shifts higher and out of the cropped images. In the C II images, the top plasma is attributed to the emission of C IV 253.0 nm.

Looking at C I distribution in Abel inverted images, there is a first order difference between measurements in air (top 2 lines) or in CO_2 (bottom 2 lines): measurements in air have a tighter distribution, whereas in CO_2, the C I emission has a larger apparent diameter. Moreover, all three configurations which have carbon in the sample have C I signal towards the center of the plasma. On the other hand, the Mg-sulfate / CO_2 configuration, where all the carbon comes from the atmosphere, has a hollow center in the C I Abel inverted images. This indicates that the C I from the sample remains close to the center of the plasma, whereas the atmospheric contribution to C I is distributed in an outer layer.

The C II distributions do not show such clear differences based on configuration, and hence origin of the carbon, although it is hard to interpret for Mg-carbonate in air, due to weak signals. In all configurations, there seems to be slightly weaker C II emissions at the center of the plasma for short delay images. This could be explained by the presence of C III in the center of the plasma at short delays, as shown in previous studies [38].

The Abel inverted data of O I (Fig. 5) all show the same distribution along a relatively thin outer envelope, farther from the sample surface than the one seen for C I in CO_2. Some differences are visible between configurations, but considering the difference in signal intensity, and thus noise level in the images, it is hard to identify anything systematic and interpretable. We thus cannot conclude that there is any significant difference in the distribution of O I observed in the different configurations.

O II distributions are tightly clustered around the center of the plasma, with a higher concentration on the edge, similar to C II. However, the shape is more elongated, less circular than for C II. Similarly to C II and O I, no clear difference in distribution depending on the configuration can be observed. The O II signal decays before the end of the s1 series and the latest images are dominated by noise.

To complement this qualitative analysis of the images, the width of each emission was extracted from the plasma imaging series (as described in the Method section), and plotted as a function of time after the laser pulse (delay, Fig. 6).

The evolution of the size of O I apparent plasma follows the same two-regime evolution described in [45], with the stagnation size being reached after about 500–700 ns. These new results are very consistent with this previous study, confirming the repeatability and robustness of the approach. That study also provides a scale for our images: the maximum size of the plasma recorded from O I emissions should be around 2.6 to 3.6 mm [45].

For O I, O II and C II, the composition of the sample and atmosphere do not appear to play a significant role on the width of the observed emissions. However, for C I, there is a significant difference between the curves corresponding to plasma developing in CO_2 (red and orange) or in air (blue), with a larger apparent width in CO_2. This is consistent with the observations of the images presented above.

Signal intensity. The image series do not clearly show the signal decay, as the color code of every image is internally normalized. To observe the changes in signal intensity, we therefore look at curves of total signal per image (as described in the Method section; Fig. 7).

The contribution of the atmosphere is most visible in the C I signal, where both CO_2 configurations have stronger C I signal than in air for most of the considered time range. Also of interest is the difference in decay for carbon-bearing and carbon-free samples for C I emissions. Measurements on Mg-sulfate, the only carbon-free sample in this study, show a continuous decrease of signal intensity for the considered time range. On the other hand, measurements on all three carbon-bearing samples show an initial fast decrease, followed by an increase of C I signal until around 0.7-1 μs, before the signal decreases for good. The C I signal is clearly weakest in the Mg-carbonate / air configuration.

The O I signal shows some variability in the decay curves resulting from the different configurations, with a seemingly monotonous decay especially for graphite in air and Mg-sulfate in CO_2, and a visible increase around 0.7-1 μs for the Mg-carbonate in air configuration. The signal is initially higher in the CO_2 configurations than the measurements in air. It is overall lowest in the graphite / air configuration, which could be expected as this is the only configuration with no oxygen in the sample. O II and C II signals show monotonous decay. These signals are overall highest in the graphite / air configuration. This might have been expected for C II but may be more surprising for O II. The overall higher signal for graphite may be explained by its lower reflectivity at the laser wavelength compared to Mg-carbonate, as well as its significantly higher absorption [50,51]. Since the refractive

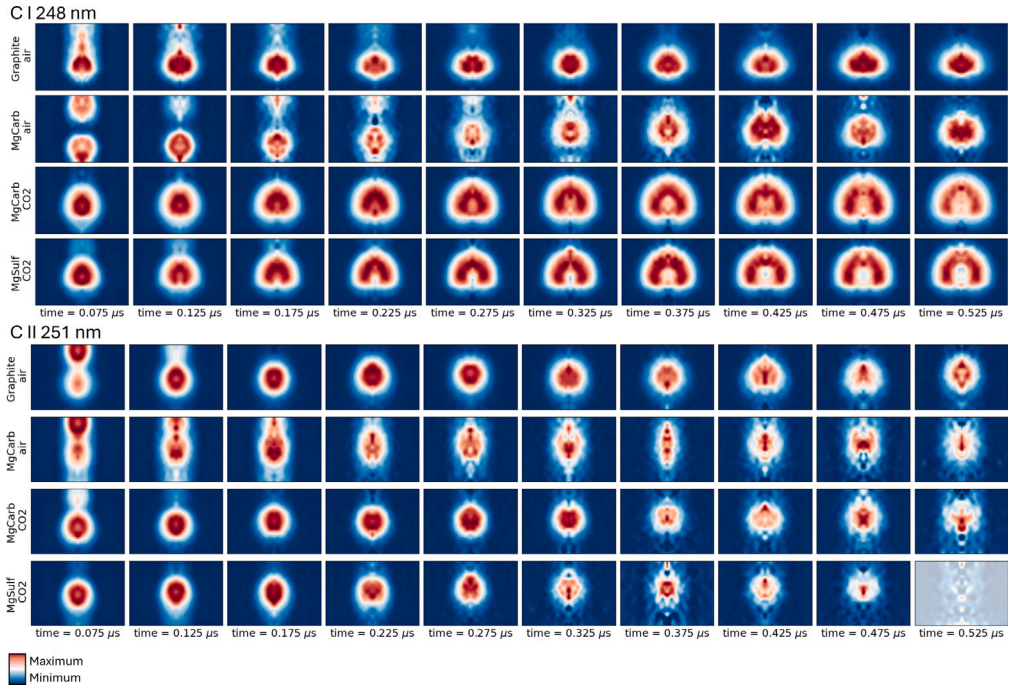

Fig. 4. C I 248 nm (top) and C II 251 nm (bottom) lines in four experimental configurations (each line): Graphite/ air, Mg-carbonate/ air, Mg-carbonate/ CO_2, Mg-sulfate/ CO_2. Smoothed and Abel inverted images. 50–500 ns delay, gate 50 ns, step 50 ns (series s1). The color range of each image is internal to maximize contrast. Images with signal below noise level are represented with transparent colors. (For interpretation of the references to color in this figure legend, the reader is referred to the web version of this article.)

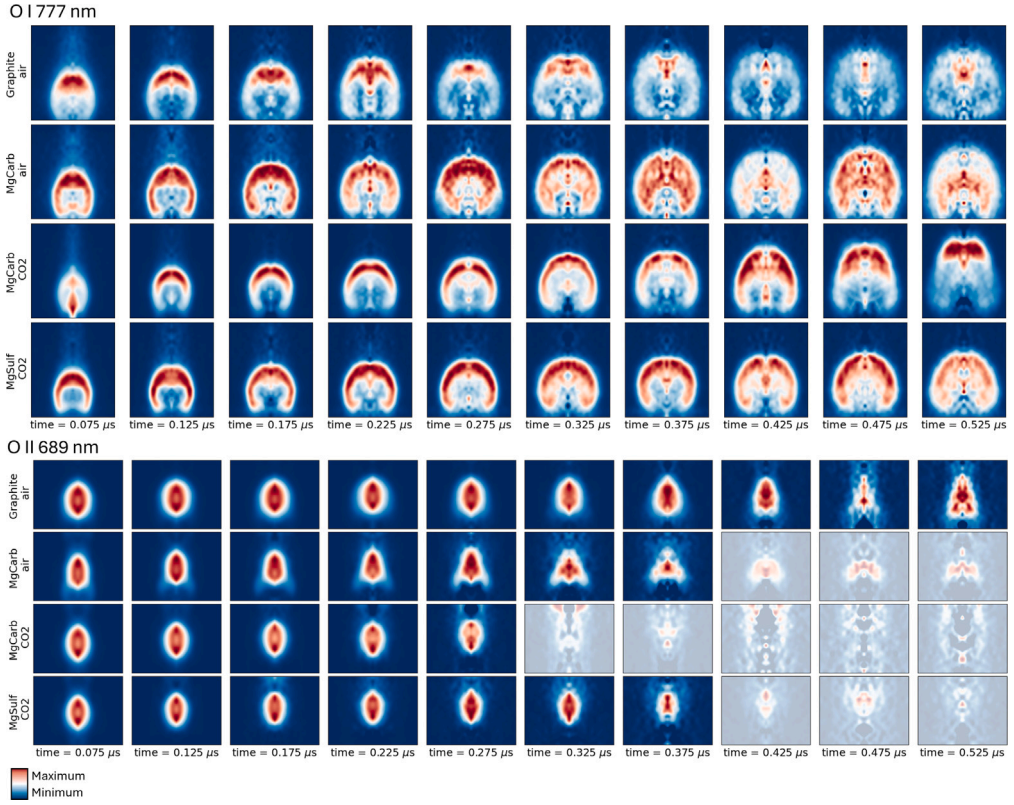

Fig. 5. O I 777 nm and O II 689 nm lines in four experimental configurations (each line): Graphite / air, Mg-carbonate / air, Mg-carbonate / CO_2, Mg-sulfate / CO_2. Smoothed and Abel inverted images. 50–500 ns delay, gate 50 ns, step 50 ns (series s1). The color range of each image is internal to maximize contrast. Images with signal below noise level are represented with transparent colors. (For interpretation of the references to color in this figure legend, the reader is referred to the web version of this article.)

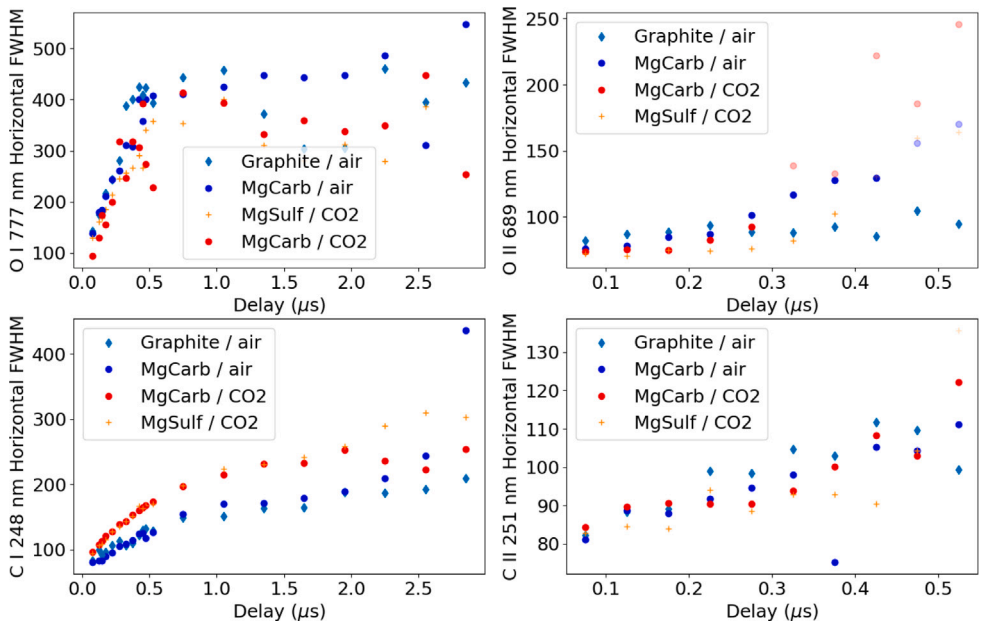

Fig. 6. Evolution of width of plasma (FWHM), parallel to sample surface, for different emission lines, through time. The unit is arbitrary, related to the pixels of the detector; images with signal below noise level are represented with transparent markers. (For interpretation of the references to color in this figure legend, the reader is referred to the web version of this article.)

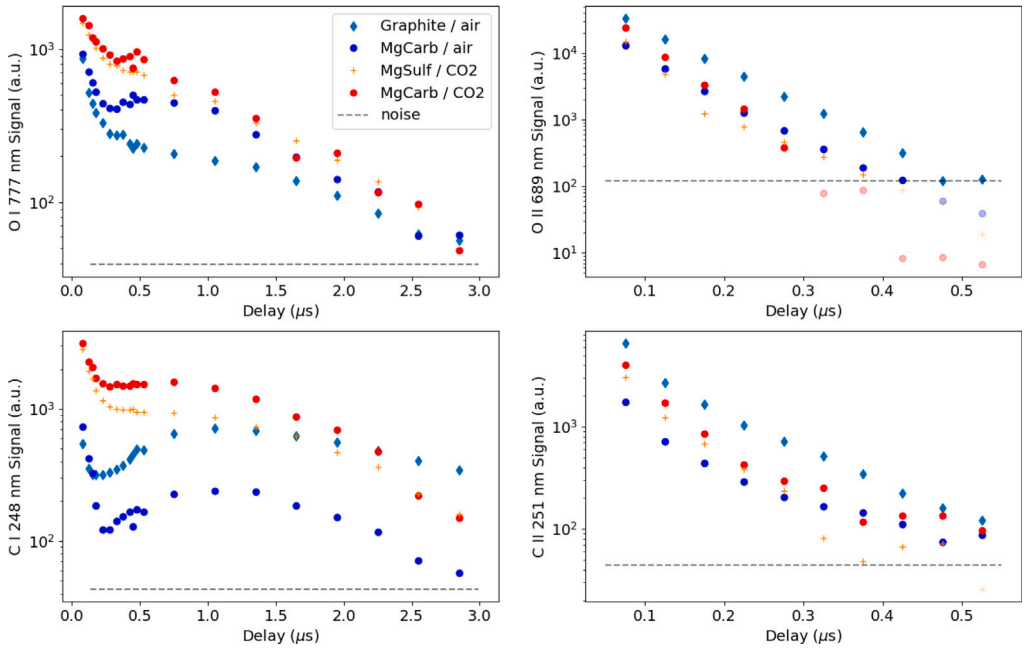

Fig. 7. Signal intensity extracted from plasma imaging series (cropped and stitched for neutral lines, before Abel inversion). The noise level of each image is represented with dashed lines; images with signal below noise level are represented with transparent markers. (For interpretation of the references to color in this figure legend, the reader is referred to the web version of this article.)

indices for these materials do not vary significantly between the visible part of the spectrum and the laser wavelength, this can also be seen directly from the perceived brightness of the sample pellets. From its visual appearance, a behavior similar to the Mg-carbonate sample may be expected for Mg-sulfate. Generally, the higher absorption coefficient of graphite leads to a smaller interaction volume in which the laser energy is deposited, increasing the local energy density in that region. This leads to enhanced heating of the material, ultimately resulting in stronger emission of ionized species. The O II signal decays the fastest and is below or around noise level for all configurations before the end of the s1 series.

Fig. 8 shows the evolution through time of ionic to neutral emissions for carbon. All curves decrease with time, due to the faster decay of ionic species compared to neutral ones. The C II / C I curves show some important differences between measurements performed in air (blue curves) and those performed in CO_2 (red and orange curves), which have significantly lower C II / C I values over the whole time range. This indicates that the atmospheric contribution to the carbon signal comes mostly in the form of C I, with a much lower relative abundance of C II than the contribution from the sample. The trends of C II / C I decay for Mg-carbonate / air and graphite / air are different, with a steeper negative slope in the graphite / air configuration. Similarly to the overall

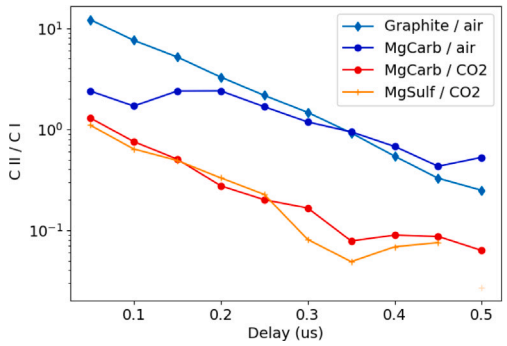

Fig. 8. Ratio of ionic to neutral signal through time for carbon for delays between 50 ns to 500 ns; images with signal below noise level are represented with transparent markers. (For interpretation of the references to color in this figure legend, the reader is referred to the web version of this article.)

stronger signal from ionized species in the graphite sample discussed above, the faster decay may be explained by the optical properties of the samples. Ablation from graphite may occur from a smaller volume, producing a plasma with stronger emission of ionized species. As the plasma expands and its energy density decreases, emission from ionized species decreases as the ions recombine with electrons [52]. For Mg-carbonate, the energy density may be lower compared to graphite, resulting in an overall lower C II / C I ratio that remains relatively stable over the first 200 ns.

Various processes, generally called matrix effects, can affect plasma emissions due to physical or chemical characteristics of the targets, affecting laser–matter interactions, plasma evolution, etc. To attenuate signal variations due to these matrix effects and enable comparison from one target to another, C-to-O ratios are most often used. They also allow to take into account the atmospheric contribution to the C signal. It was showed that it is best practice to normalize lines of the same ionization degree, otherwise the ratio is very dependent on parameters such as the laser irradiance [33,41]. We therefore look at the evolutions of the C I / O I and C II / O II ratios through time, in the four experimental configurations of this study. Since C I lines are generally hard to use in Martian LIBS data, C II lines are most often used, normalized to the O I signal [4,8,39], so we also investigate this ratio (Fig. 9).

The C I / O I ratios are about one order of magnitude lower for Mg-carbonate in air compared to measurements on the same sample in CO_2, showing again how significant the atmospheric contribution is (Fig. 9). Looking at the two measurements performed in CO_2, the C I / O I ratio is higher in Mg-carbonate than Mg-sulfate over most of the time series, which is expected and consistent with the approach used in several studies [8,39], but the difference is a factor 2 at most and lower for most of the considered time range. For measurements in air, graphite leads to much higher C I / O I ratio for most of the time series, even higher than those in CO_2 after a few hundred ns.

C II / O II show similar behaviors for all four configurations, so long as the signal is sufficient (opaque vs transparent markers; Fig. 7). Surprisingly, the C II / O II ratio is higher in Mg-sulfate than Mg-carbonate for the CO_2 measurements between 50 and 200 ns.

C II / O I ratios decrease with time, due to the faster decay of ionized lines compared to neutral ones. The measurements for graphite in air show higher C II / O I ratios than the other three configurations (factor 5). Those show roughly similar C II / O I ratios, with both Mg-carbonate configurations only slightly above the configuration with Mg-sulfate in CO_2.

Finally, to enable comparison with the signals extracted from ChemCam or SuperCam LIBS spectra on Mars, which have long integration gates ($\geq$ 100 µs, [22,25]), we integrate the signal acquired for each emission line of the whole time range covered by the time series (described in Method section). The time-integrated signals, and ratios of these signals are shown in Fig. 10.

The time-integrated C I and O I signals are highest in CO_2 measurements, for carbonate, then sulfate, followed by measurements in air. Singly ionic emissions are highest in the graphite / air configuration, for both carbon and oxygen, probably due to the darker color of that graphite pellet leading to higher laser absorption and hence higher temperatures. The second highest C II and O II signals are found for carbonate in CO_2.

In practice, absolute signal intensities are rarely usable for in situ geologic analysis, as they are affected by multiple matrix effects. Normalization is used to attenuate these effects and enable signal comparison from one target to the other. Out of the three plotted C / O ratios, two are higher for the carbonate than the sulfate in CO_2 (red circle vs orange plus): C I / O I and C II / O I, which are both about 25% higher in carbonate compared to sulfate. It is unclear why the C II / O II ratio is not higher for carbonate than sulfate in CO_2.

4. Discussion

Technical aspects. Even though we chose the simplest possible samples for this study to make comparison easier, matrix effects are not entirely ruled out: the graphite is dark gray whereas the other two are white, likely affecting laser absorption. This appears to lead to higher initial plasma temperatures and hence higher ionic to neutral ratio on this sample. Another aspect is related to water content: we first worked with an anhydrous sulfate powder, but it had larger grains than the other powders, and was unstable: absorbing water and thus expanding significantly. To mitigate these effects, we decided to use a Mg-sulfate with 1 H_2O in the structure. The water might lead to slightly different matrix effects, but the pellet being more stable and of similar grain size than the others was considered the more important aspect.

Regarding the data acquisition procedure, one limitation of the method is that we are not measuring the exact same plasma through its entire lifetime but collecting data from many plasmas. The signal is accumulated from 10 distinct laser-induced plasmas for each measurement, and then comparing distinct measurements such as two different heights or different emission lines. Although we did our best to make measurements as repeatable as possible so that plasma characteristics and emissions are similar between measurements, the observations for one nominal configuration did not always match perfectly. The solution which is most often used in LIBS spectroscopy to improve repeatability is signal normalization, but it is not applicable in this case, for the same reasons. The main factors that might affect the repeatability are:

- local changes in surface characteristics of the sample (roughness, hydration, ...), although this was mitigated as much as possible by using pure pellets, prepared in the same way, with homogeneous powders, and moving the laser beam on the surface of the sample throughout measurements to ablate pristine surfaces with each pulse.
- slight changes in pressure: in some cases, we noticed degassing leading to an increasing pressure in the experimental chamber (1 mbar in a couple of hours). The pressure was controlled and adjusted regularly if needed to remain between 6 and 7 mbar for all measurements, to limit this effect.
- the wavelength calibration in the spectrometer used in this study is not entirely stable when switching gratings, leading to small shifts in wavelength calibration. This is not too critical in this study, which focuses on specific and isolated lines, but might lead to uncertainties in the line positions in the presented spectra.

We also highlight the challenge of finding suitable lines for plasma imaging studies, with the need for sufficient signal and sufficiently isolated lines. We were not able to work with the C II lines which are most often used with in situ LIBS data from Mars, but assume that

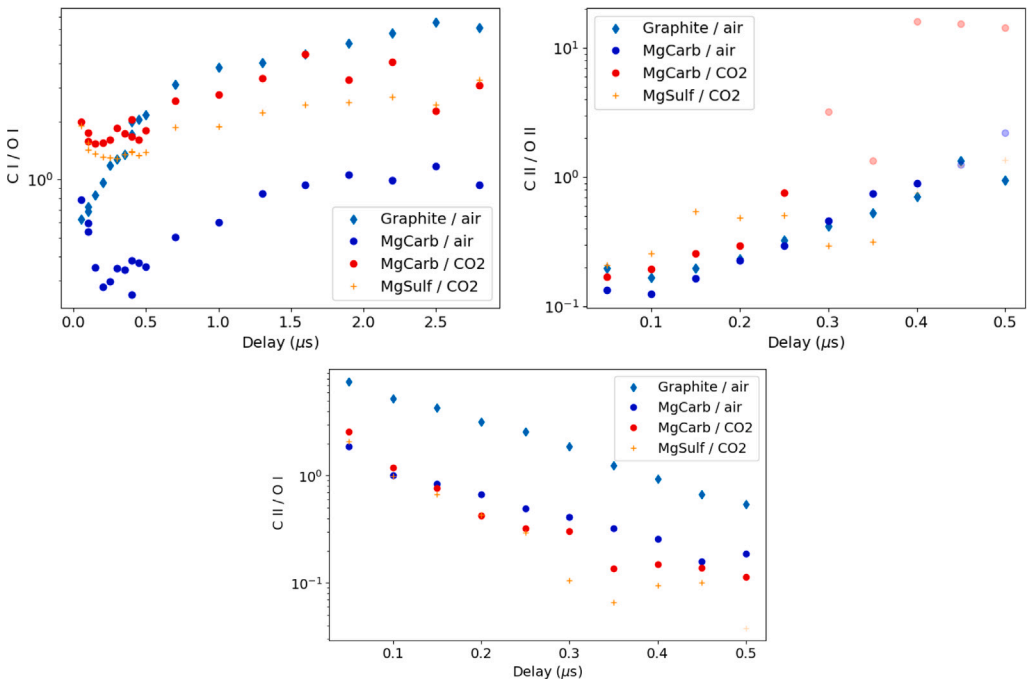

Fig. 9. C-to-O ratios through time: C I / O I, C II / O II and C II / O I. Images with signal below noise level for one of the two lines are represented with transparent markers.

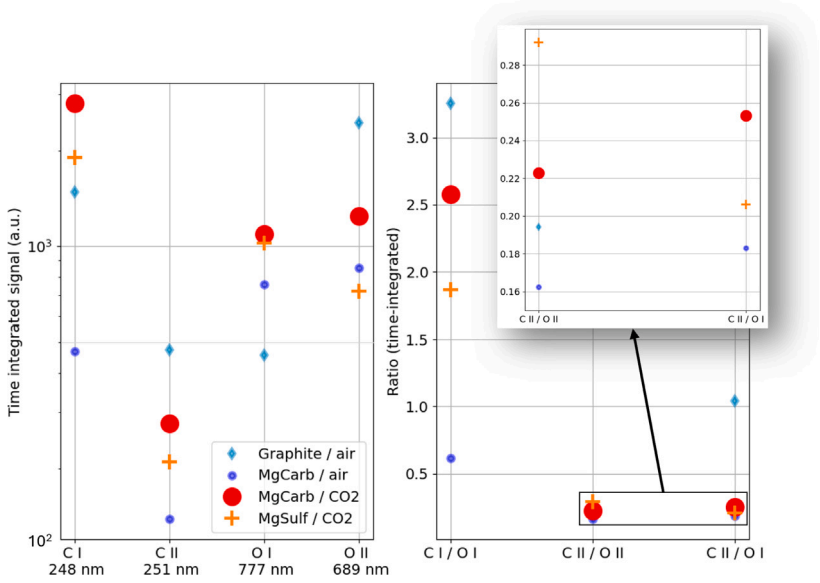

Fig. 10. Time-integrated signal per emission line (left, logarithmic scale) and ratios of these signals (right). (For interpretation of the references to color in this figure legend, the reader is referred to the web version of this article.)

the lines used in this study are representative of the populations of interest, namely C I, C II, O I and O II. Going back to Mars data, it is likely that some of the lines used in this study will not be usable, due to the characteristics of the spectrometers onboard the Martian rovers and the emission line intensities in the time-integrated mission data or being superimposed by other emission lines.

Atmospheric contributions to plasma emissions. Overall, we observe a significant contribution of the atmosphere to the carbon and oxygen signal, in terms of intensity, decay and distribution, especially for neutral emission lines.

The atmospheric contribution to carbon emissions appears to come with a high neutral to ionized ratio. This is observed in the significant difference between measurements in air and CO_2 in the C I decay curves, as well as in the C II / C I ratio. This is understandable since carbon coming from the breakdown of atmospheric CO_2 molecules results from plasma–atmosphere interactions rather than direct heating of the sample by the laser. It thus comes at lower temperature, consistent with the higher abundance of neutral carbon. With this relatively low C II / C I in atmospheric contribution, evidence of recombination of C II to C I is very small for atmospheric contribution whereas it is strong for sample contribution, observed as a “bump” in the C I decay curves, corresponding to the C I population being replenished by this process. Moreover, the spatial distributions of C I from atmospheric and sample sources appear distinct, with the atmospheric C I being in an outer part of the plasma compared to the sample contribution which stays close to

the center. Such difference in spatial distribution for atmospheric and sample contributions is not observed for the other species investigated in this study, neither is any strong difference in decay curve, etc. for the singly ionized species.

Based on the results of this study, it is recommended to use carbon neutral emission when possible to characterize a sample's carbon content, as most of the differences between atmospheric and sample contributions are visible in these emissions. With access to time series, modeling the C I decay curve as the sum of a direct decay and the recombination of C II in C I might help separate the sample and atmospheric contributions (to be investigated), since the sample appears to be contributing most of the recombining C II. Otherwise, the C I / O I ratio has the highest relative contribution from the sample. However, the C I 248 nm emission line is not usable in most cases on Mars due to the overlap of iron lines around and on top of this C I line [33], which is problematic when most of the carbonates detected in situ on Mars so far are Fe-bearing [3,4,8,53]. One way to use this emission line could be to use spectral unmixing/modeling, taking into account surrounding lines to accurately separate the Fe and C contributions, rather than with univariate fits [54]. Otherwise, one would have to use C II lines, as done in most Martian in situ LIBS studies; in that case, normalizing to O I seems to be more efficient than normalizing to O II, although one would then have to be careful to take into account any influence of laser irradiance, timing, etc. For both C I / O I and C II / O I ratios, the sample contribution is in the order of 20%–25% of the signal for the pure carbonate samples analyzed in this study. For carbonates mixed in other substances, it is therefore expected that the carbon contribution of the sample would be challenging to identify clearly, consistently with previous work [39].

The heterogeneity of the plasma, especially the different spatial distribution of neutral and ionized species (consistent with previous plasma imaging studies as [38]), or sample and atmospheric contributions (this study), highlights how important it is to collect emissions from the entire plasma when generating a LIBS spectrum, to accurately document species ratio and plasma characteristics. In particular, this must be especially taken into account when designing instruments for measurements in different atmospheric conditions, as documented in [45].

5. Conclusion

Despite the contribution of the Martian atmosphere (96% CO_2) to the carbon signal in Martian LIBS, it remains the only technique with the potential for in situ characterization, and even possibly quantification of carbon remotely, under an hour and without sample preparation. To reach the full potential of LIBS on that topic, further studies are necessary, to better understand the plasma–atmosphere interactions and hence better account for this atmospheric contribution. This study is a first step in that direction.

Using a unique plasma imaging setup combined with a vacuum chamber to experimentally simulate Martian atmospheric conditions, we investigated the spatial and temporal dynamics of carbon and oxygen in the laser-induced plasma, depending on their origin, from the sample or the atmosphere. We highlight some characteristics of the emissions originating from the atmosphere, such as a low C II / C I ratio, subsequent weak recombination of C II to C I observed in the C I decay curve, and a distinct spatial distribution of the C I emissions compared to those originating from the sample. Based on the results of this study, it appears most efficient to use C I / O I or C II / O I ratios to distinguish the contribution of carbon from the sample, such as in form of carbonates, from carbon from the breakdown of the CO_2-dominated Martian ambient atmosphere.

CRediT authorship contribution statement

E. Clavé: Writing – review & editing, Writing – original draft, Visualization, Validation, Methodology, Investigation, Formal analysis, Data curation, Conceptualization. **K. Rammelkamp:** Writing – review & editing, Validation, Supervision, Resources, Funding acquisition, Conceptualization. **F. Seel:** Writing – review & editing, Validation, Methodology, Investigation. **P. Hansen:** Writing – review & editing, Validation, Investigation. **C.H. Egerland:** Writing – review & editing, Investigation. **S. Schröder:** Writing – original draft, Validation, Supervision, Resources, Investigation, Funding acquisition, Conceptualization.

Declaration of competing interest

The authors declare that they have no known competing financial interests or personal relationships that could have appeared to influence the work reported in this paper.

Appendix A. Supplementary data

Supplementary material related to this article can be found online at https://doi.org/10.1016/j.sab.2026.107537.

Data availability

Data will be made available on request.

References

[1] J. Bridges, L.J. Hicks, A.H. Treiman, Carbonates on Mars, in: Volatiles in the Martian Crust, Elsevier, 2019, pp. 89–118, http://dx.doi.org/10.1016/B978-0-12-804191-8.00005-2.

[2] B. Ehlmann, J.F. Mustard, G.A. Swayze, R.N. Clark, J.L. Bishop, F. Poulet, D.J.D. Marais, L.H. Roach, R.E. Milliken, J.J. Wray, O. Barnouin-Jha, S.L. Murchie, Identification of hydrated silicate minerals on mars using MRO-CRISM: Geologic context near Nili Fossae and implications for aqueous alteration, J. Geophys. Res.: Planets 114 (2009) http://dx.doi.org/10.1029/2009JE003339.

[3] B.M. Tutolo, E.M. Hausrath, E.S. Kite, E.B. Rampe, T.F. Bristow, R.T. Downs, A. Treiman, T.S. Peretyazhko, M.T. Thorpe, J.P. Grotzinger, A.L. Roberts, P.D. Archer, D.J.D. Marais, D.F. Blake, D.T. Vaniman, S.M. Morrison, S. Chipera, R.M. Hazen, R.V. Morris, V.M. Tu, S.L. Simpson, A. Pandey, A. Yen, S.R. Larter, P. Craig, N. Castle, D.W. Ming, J.M. Meusburger, A.A. Fraeman, D.G. Burtt, H.B. Franz, B. Sutter, J.V. Clark, W. Rapin, J.C. Bridges, M. Loche, P. Gasda, J. Frydenvang, A.R. Vasavada, Carbonates identified by the curiosity rover indicate a carbon cycle operated on ancient Mars, Science 388 (6744) (2025) 292–297, http://dx.doi.org/10.1126/science.ado9966.

[4] E. Clave, O. Beyssac, P. Beck, C. Royer, L. Mandon, N. Mangold, O. Forni, E. Dehouck, C. Bedford, A. Udry, S. Schroeder, S. Bernard, C. Quantin-Natf, M. Loche, J. Aramendia, A. Brown, G. Caravaca, et al., In situ carbonation of igenous and sedimentary rocks of ultramafic composition in Jezero Crater, Mars, J. Geophys. Res.: Planets http://dx.doi.org/10.1029/2025JE009107.

[5] R. Morris, S.W. Ruff, R. Gellert, D.W. Ming, R.E. Arvidson, B.C. Clark, D.C. Golden, K. Siebach, G. Klingelhoefer, C. Schroeder, I. Fleischer, A.S. Yen, S.W. Squyres, Identification of carbonate-rich outcrops on Mars by the spirit rover, Science 329 (5990) (2010) 421–424, http://dx.doi.org/10.1126/science.1189667.

[6] L. Mandon, C. Quantin-Nataf, C. Royer, P. Beck, T. Fouchet, J. Johnson, E. Dehouck, S. Le Mouelic, F. Poulet, F. Montmessin, C. Pilorget, O. Gasnault, O. Forni, L. Mayhew, O. Beyssac, T. Bertrand, P. PInet, C. Legett, A. Brown, J. Tarnas, E. Cloutis, G. Poggiali, T. Fornaro, S. Maurice, R. Wiens, the SuperCam team, Reflectance of Jezero crater floor: 2, J. Geophys. Res.: Planets (2022).

[7] C. Royer, F. Poulet, R. Wiens, F. Montmession, P. Beck, O. Beyssac, E. Clave, E. Dehouck, T. Fouchet, J. Johnson, L. Mandon, S. Bernard, G. Caravaca, S. le Mouelic, C. Pilorget, C. Quantin-Nataf, S. Maurice, A. Cousin, The mineralogical composition of Jezero Crater Western Fan: Multigaussian modeling of Perseverance/SuperCam near-infrared observations and overview of major units, Icarus (2025) http://dx.doi.org/10.1016/j.icarus.2025.116538.

[8] E. Clave, K. Benzerara, P.Y. Meslin, O. Forni, C. Royer, L. Mandon, P. Beck, C. Quantin-Nataf, O. Beyssac, A. Cousin, B. Bousquet, R. Wiens, S. Maurice, E. Dehouck, S. Schroeder, O. Gasnault, N. Mangold, G. Dromart, T. Bosak, S. Bernad, A. Udry, R. Anderson, G. Arana, A. Brown, K. Castro, S. Clegg, E. Cloutis, A. Fairen, D. Flannery, P. Gasda, J. Johnson, J. Lasue, G. Lopez-Reyes, J. Madariaga, J. Manrique, S. Le Mouelic, J. Nunez, A. Ollila, P. Pilleri, C. Pilorget, P. Pinet, F. Poulet, M. Veneranda, Z. Wolf, the SuperCam Team, Carbonate detection with SuperCam in igneous rocks on the floor of Jezero crater, Mars, J. Geophys. Res.: Planets (2023) http://dx.doi.org/10.1029/2022JE007463.

[9] A. Corpolongo, R. Jakubek, W. Abbey, S. Asher, D. Baker, L. Beegle, E. Berger, R. Bhartia, A. Brown, A. Burton, S. Bykov, E. Cardarelli, E. Cloutis, P. Conrad, A. Czaja, L. DeFlores, D. Flannery, T. Fornaro, M. Fries, N. Haney, K. Hickman-Lewis, L. Kah, C. Lee, F. McCubbin, M. Minitti, R. Morris, J. Razzell Hollis, R. Roppel, E. Scheller, S. Sharma, S. Shkolyar, S. Siljestroem, K. Steadman, A. Steele, K. Uckert, B. Wogsland, A. Yanchilina, SHERLOC Raman mineral detections of the Mars 2020 Crater Floor Campaign, J. Geophys. Res.: Planets (2022).

[10] E. Moreland, K. Siebach, G. Costin, M. Tice, J. Hurowitz, A. Treiman, J. Simon, Y. Liu, Y. Jiang, A. Udry, E. Dehouck, Multiple episodes of fluid alteration in Jezero crater indicated by MIST mineral identifications in PIXL XRF data from the first 1100 sols of the mars 2020 mission, J. Geophys. Res.: Planets (2025) http://dx.doi.org/10.1029/2024JE008797.

[11] J. Christian, S. VanBommel, T. Kizovski, Y. Liu, M. Schmidt, Characterization of composition endmembers in PIXL scans, Icarus (2026) http://dx.doi.org/10.1016/j.icarus.2026.117060.

[12] C. Freissinet, D. Glavin, P. Mahaffy, K. Miller, J. Eigenbrode, R. Summons, A. Brunner, A. Buch, C. Szopa, P.J. Archer, H. Franz, et al., Organic molecules in the Sheepbed Mudstone, Gale Crater, Mars, J. Geophys. Res.: Planets (2015) http://dx.doi.org/10.1002/2014je004737.

[13] C. Szopa, C. Freissinet, D. Glavin, M. Millan, A. Buch, H. Franz, R. Summons, D. Sumner, B. Sutter, J. Eigenbrode, R. Williams, R. Navarro-González, M. Guzman, C. Malespin, S. Teinturier, P. Mahaffy, M. Cabane, First detections of dichlorobenzene isomers and trichloromethylpropane from organic matter indigenous to Mars mudstone in Gale crater, Mars: Results from the sample analysis at Mars instrument onboard the curiosity rover, Astrobiology (2020) http://dx.doi.org/10.1089/ast.2018.1908.

[14] J. Stern, C. Malespin, J. Eigenbrode, C. Webster, G. Flesch, H. Franz, H. Graham, C. House, C.e.a. Sutter, Organic carbon concentrations in 3.5-billion-year-old lacustrine mudstones on Mars, PNAS (2022) http://dx.doi.org/10.1073/pnas.2201139119.

[15] S. Sharma, R.D. Roppel, A.E. Murphy, L.W. Beegle, R. Bhartia, A. Steele, J.R. Hollis, S. Siljestrom, F.M. McCubbin, S.A. Asher, W.J. Abbey, A.C. Allwood, E.L. Berger, B.L. Bleefeld, A.S. Burton, S.V. Bykov, E.L. Cardarelli, P.G. Conrad, A. Corpolongo, A.D. Czaja, L.P. DeFlores, K. Edgett, K.A. Farley, T. Fornaro, A.C. Fox, M.D. Fries, D. Harker, K. Hickman-Lewis, J. Huggett, S. Imbeah, R.S. Jakubek, L.C. Kah, C. Lee, Y. Liu, A. Magee, M. Minitti, K.R. Moore, A. Pascuzzo, C. Rodriguez Sanchez-Vahamonde, E.L. Scheller, S. Shkolyar, K.M. Stack, K. Steadman, M. Tuite, K. Uckert, A. Werynski, R.C. Wiens, A.J. Williams, K. Winchell, M.R. Kennedy, A. Yanchilina, Diverse organic-mineral associations in Jezero crater, Mars, Nature 619 (7971) (2023) 724–732, http://dx.doi.org/10.1038/s41586-023-06143-z.

[16] T. Fornaro, S. Sharma, R.S. Jakubek, G. Poggiali, J.R. Brucato, R. Bhartia, A. Steele, A.E. Murphy, M.M. Tice, M.D. Schulte, K.P. Hand, M.D. Fries, W.J. Abbey, A. Alberini, D. Alvarado-Jiménez, K.C. Benison, E.L. Berger, S. Biancalani, A.J. Brown, A.P. Broz, W.P. Buckley, D.K. Buckner, A.S. Burton, S.V. Bykov, E.L. Cardarelli, E.A. Cloutis, S.A. Connell, C. Garcia-Florentino, F. Gómez, N.C. Haney, C. Lee, V. Lino, P. Manini, F.M. McCubbin, M.E. Minitti, R.V. Morris, Y.Y. Phua, N. Randazzo, J. Razzell Hollis, F. Renzi, S. Siljeström, J.I. Simon, A. Srivastava, N. Tasinato, K. Uckert, R.C. Wiens, A.J. Williams, Evidence for polycyclic aromatic hydrocarbons detected in sulfates at Jezero crater by the Perseverance rover, Nat. Astron. 9 (11) (2025) 1648–1661, http://dx.doi.org/10.1038/s41550-025-02638-z.

[17] G. Klingelhoefer, R.V. Morris, B. Bernhardt, D. Rodionov, P.A. de Souza Jr., S.W. Squyres, J. Foh, E. Kankeleit, U. Bonnes, R. Gellert, C. Schroeder, S. Linkin, E. Evlanov, B. Zubkov, O. Prilutski, Athena MIMOS II Moessbauer spectrometer investigation, J. Geophys. Res.: Planets 108 (E12) (2003) http://dx.doi.org/10.1029/2003JE002138.

[18] J. Grotzinger, J. Crisp, A. Vasavada, R. Anderson, C. Baker, Mars science laboratory mission and science investigation, Space Sci. Rev. (2012) http://dx.doi.org/10.1007/s11214-012-9892-2.

[19] J. Blacic, D. Pettit, D. Cremers, N. Roessler, Laser-Induced Breakdown Spectroscopy Instrument for Elemental Analysis on Planetary Surfaces, LPI Technical Report 93-02, 1993.

[20] R. Brennetot, J.L. Lacour, E. Vors, A. Rivoallan, D. Vailhen, S. Maurice, Mars analysis by laser-induced breakdown spectroscopy (MALIS): Influence of mars atmosphere on plasma emission and study of factors influencing plasma emission with the use of doehlert designs, Appl. Spectrosc. 57 (7) (2003) 744–752, http://dx.doi.org/10.1366/000370203322102816.

[21] R.C. Wiens, R.E. Arvidson, D.A. Cremers, M.J. Ferris, J.D. Blacic, F.P. Seelos, K.S. Deal, Combined remote mineralogical and elemental identification from rovers: Field and laboratory tests using reflectance and laser-induced breakdown spectroscopy: identification using reflectance and LIBS, J. Geophys. Res.: Planets 107 (E11) (2002) FIDO 3–1–FIDO 3–14, http://dx.doi.org/10.1029/2000JE001439.

[22] R. Wiens, S. Maurice, B. Barraclough, M. Saccoccio, W. Barkley, J.F. Bell, S. Bender, J. Bernardin, D. Blaney, J. Blank, M. Bouye, N. Bridges, N. Bultman, P. Caïs, R.C. Clanton, B. Clark, S. Clegg, A. Cousin, D. Cremers, A. Cros, L. DeFlores, D. Delapp, R. Dingler, C. D'Uston, M. Darby Dyar, T. Elliott, D. Enemark, C. Fabre, M. Flores, O. Forni, O. Gasnault, T. Hale, C. Hays, K. Herkenhoff, E. Kan, L. Kirkland, D. Kouach, D. Landis, Y. Langevin, N. Lanza, F. LaRocca, J. Lasue, J. Latino, D. Limonadi, C. Lindensmith, C. Little, N. Mangold, G. Manhes, P. Mauchien, C. McKay, E. Miller, J. Mooney, R. Morris, L. Morrison, T. Nelson, H. Newsom, A. Ollila, M. Ott, L. Pares, R. Perez, F. Poitrasson, C. Provost, J.W. Reiter, T. Roberts, F. Romero, V. Sautter, S. Salazar, J.J. Simmonds, R. Stiglich, S. Storms, N. Striebig, J.J. Thocaven, T. Trujillo, M. Ulibarri, D. Vaniman, N. Warner, R. Waterbury, R. Whitaker, J. Witt, B. Wong-Swanson, The ChemCam instrument suite on the Mars science laboratory (MSL) rover: Body unit and combined system tests, Space Sci. Rev. 170 (1–4) (2012) 167–227, http://dx.doi.org/10.1007/s11214-012-9902-4.

[23] S. Maurice, R.C. Wiens, M. Saccoccio, B. Barraclough, O. Gasnault, O. Forni, N. Mangold, D. Baratoux, S. Bender, G. Berger, J. Bernardin, M. Berthe, N. Bridges, D. Blaney, M. Bouye, P. Caïs, B. Clark, S. Clegg, A. Cousin, D. Cremers, A. Cros, L. DeFlores, C. Derycke, B. Dingler, G. Dromart, B. Dubois, M. Dupieux, E. Durand, L. d'Uston, C. Fabre, B. Faure, A. Gaboriaud, T. Gharsa, K. Herkenhoff, E. Kan, L. Kirkland, D. Kouach, J.L. Lacour, Y. Langevin, J. Lasue, S. Le Mouelic, M. Lescure, E. Lewin, D. Limonadi, G. Manhes, P. Mauchien, C. McKay, P.Y. Meslin, Y. Michel, E. Miller, H.E. Newsom, G. Orttner, A. Paillet, L. Pares, Y. Parot, R. Perez, P. Pinet, F. Poitrasson, B. Quertier, B. Salle, C. Sotin, V. Sautter, H. Seran, J.J. Simmonds, J.B. Sirven, R. Stiglich, N. Striebig, J.J. Thocaven, M.J. Toplis, D. Vaniman, The ChemCam instrument suite on the Mars science laboratory (MSL) rover: Science objectives and mast unit description, Space Sci. Rev. 170 (1–4) (2012) 95–166, http://dx.doi.org/10.1007/s11214-012-9912-2.

[24] W. Xu, X. Liu, Z.e.a. Yan, The MarSCoDe instrument suite on the Mars rover of China's Tianwen-1 mission, Space Sci. Rev. (2021) http://dx.doi.org/10.1007/s11214-021-00836-5.

[25] R. Wiens, S. Maurice, S.H. Robinson, A. Nelson, P. Cais, P. Bernardi, R.T. Newell, S. Clegg, S.K. Sharma, S. Storms, J. Deming, D. Beckman, A.M. Ollila, O. Gasnault, R.B. Anderson, Y. Andre, S. Michael Angel, G. Arana, E. Auden, P. Beck, J. Becker, K. Benzerara, S. Bernard, O. Beyssac, L. Borges, B. Bousquet, K. Boyd, M. Caffrey, J. Carlson, K. Castro, J. Celis, B. Chide, K. Clark, E. Cloutis, E.C. Cordoba, A. Cousin, M. Dale, L. Deflores, D. Delapp, M. Deleuze, M. Dirmyer, C. Donny, G. Dromart, M. George Duran, M. Egan, J. Ervin, C. Fabre, A. Fau, W. Fischer, O. Forni, T. Fouchet, R. Fresquez, J. Frydenvang, D. Gasway, I. Gontijo, J. Grotzinger, X. Jacob, S. Jacquinod, J.R. Johnson, R.A. Klisiewicz, J. Lake, N. Lanza, J. Laserna, J. Lasue, S. Le Mouelic, C. Legett, R. Leveille, E. Lewin, G. Lopez-Reyes, R. Lorenz, E. Lorigny, S.P. Love, B. Lucero, J.M. Madariaga, M. Madsen, S. Madsen, N. Mangold, J.A. Manrique, J.P. Martinez, J. Martinez-Frias, K.P. McCabe, T.H. McConnochie, J.M. McGlown, S.M. McLennan, N. Melikechi, P.Y. Meslin, J.M. Michel, D. Mimoun, A. Misra, G. Montagnac, F. Montmessin, V. Mousset, N. Murdoch, H. Newsom, L.A. Ott, Z.R. Ousnamer, L. Pares, Y. Parot, R. Pawluczyk, C. Glen Peterson, P. Pilleri, P. Pinet, G. Pont, F. Poulet, C. Provost, B. Quertier, H. Quinn, W. Rapin, J.M. Reess, A.H. Regan, A.L. Reyes-Newell, P.J. Romano, C. Royer, F. Rull, B. Sandoval, J.H. Sarrao, V. Sautter, M.J. Schoppers, S. Schroeder, D. Seitz, T. Shepherd, P. Sobron, B. Dubois, V. Sridhar, M.J. Toplis, I. Torre-Fdez, I.A. Trettel, M. Underwood, A. Valdez, J. Valdez, D. Venhaus, P. Willis, The SuperCam instrument suite on the NASA Mars 2020 rover: Body unit and combined system tests, Space Sci. Rev. 217 (1) (2021) 4, http://dx.doi.org/10.1007/s11214-020-00777-5.

[26] S. Maurice, R.C. Wiens, P. Bernardi, P. Caïs, S. Robinson, T. Nelson, O. Gasnault, J.M. Reess, M. Deleuze, F. Rull, J.A. Manrique, S. Abbaki, R.B. Anderson, Y. Andre, S.M. Angel, G. Arana, T. Battault, P. Beck, K. Benzerara, S. Bernard, J.P. Berthias, O. Beyssac, M. Bonafous, B. Bousquet, M. Boutillier, A. Cadu, K. Castro, F. Chapron, B. Chide, K. Clark, E. Clave, S. Clegg, E. Cloutis, C. Collin, E.C. Cordoba, A. Cousin, J.C. Dameury, W. D'Anna, Y. Daydou, A. Debus, L. Deflores, E. Dehouck, D. Delapp, G. De Los Santos, C. Donny, A. Doressoundiram, G. Dromart, B. Dubois, A. Dufour, M. Dupieux, M. Egan, J. Ervin, C. Fabre, A. Fau, W. Fischer, O. Forni, T. Fouchet, J. Frydenvang, S. Gauffre, M. Gauthier, V. Gharakanian, O. Gilard, I. Gontijo, R. Gonzalez, D. Granena, J. Grotzinger, R. Hassen-Khodja, M. Heim, Y. Hello, G. Hervet, O. Humeau, X. Jacob, S. Jacquinod, J.R. Johnson, D. Kouach, G. Lacombe, N. Lanza, L. Lapauw, J. Laserna, J. Lasue, L. Le Deit, S. Le Mouelic, E. Le Comte, Q.M. Lee, C. Legett, R. Leveille, E. Lewin, C. Leyrat, G. Lopez-Reyes, R. Lorenz, B. Lucero, J.M. Madariaga, S. Madsen, M. Madsen, N. Mangold, F. Manni, J.F. Mariscal, J. Martinez-Frias, K. Mathieu, R. Mathon, K.P. McCabe, T. McConnochie, S.M. McLennan, J. Mekki, N. Melikechi, P.Y. Meslin, Y. Micheau, Y. Michel, J.M. Michel, D. Mimoun, A. Misra, G. Montagnac, C. Montaron, F. Montmessin, J. Moros, V. Mousset, Y. Morizet, N. Murdoch, R.T. Newell, H. Newsom, N. Nguyen Tuong, A.M. Ollila, G. Orttner, L. Oudda, L. Pares, J. Parisot, Y. Parot, R. Perez, D. Pheav, L. Picot, P. Pilleri, C. Pilorget, P. Pinet, G. Pont, F. Poulet, C. Quantin-Nataf, B. Quertier, D. Rambaud, W. Rapin, P. Romano, L. Roucayrol, C. Royer, M. Ruellan, B.F. Sandoval, V. Sautter, M.J. Schoppers, S. Schroeder, H.C. Seran, S.K. Sharma, P. Sobron, M. Sodki, A. Sournac, V. Sridhar, D. Standarovsky, S. Storms, N. Striebig, M. Tatat, M. Toplis, I. Torre-Fdez, N. Toulemont, C. Velasco, M. Veneranda, D. Venhaus, C. Virmontois, M. Viso, P. Willis, K.W. Wong, The SuperCam instrument suite on the Mars 2020 rover: Science objectives and mast-unit description, Space Sci. Rev. 217 (3) (2021) 47, http://dx.doi.org/10.1007/s11214-021-00807-w.

[27] S.M. Clegg, R. Wiens, R. Anderson, O. Forni, J. Frydenvang, J. Lasue, A. Cousin, V. Payre, T. Boucher, M.D. Dyar, S.M. McLennan, R. Morris, T.G. Graff, S.A. Mertzman, B. Ehlmann, I. Belgacem, H. Newsom, B.C. Clark, N. Melikechi, A. Mezzacappa, R.E. McInroy, R. Martinez, P. Gasda, O. Gasnault, S. Maurice, Recalibration of the Mars science laboratory ChemCam instrument with an

expanded geochemical database, Spectrochim. Acta Part B: At. Spectrosc. 129 (2017) 64–85, http://dx.doi.org/10.1016/j.sab.2016.12.003.

[28] R. Anderson, O. Forni, A. Cousin, R. Wiens, S. Clegg, J. Frydenvang, T.S. Gabriel, A. Ollila, S. Schroeder, O. Beyssac, E. Gibbons, D.S. Vogt, E. Clave, J.A. Manrique, I. Carey Legett, P. Pilleri, R.T. Newell, J. Sarrao, S. Maurice, G. Arana, K. Benzerara, P. Bernardi, S. Bernard, B. Bousquet, A.J. Brown, C. Alvarez-Llamas, B. Chide, E. Cloutis, J. Comellas, S. Connell, E. Dehouck, D.M. Delapp, A. Essunfeld, C. Fabre, T. Fouchet, C. Garcia-Florentino, L. García-Gomez, P. Gasda, O. Gasnault, E.M. Hausrath, N.L. Lanza, J. Laserna, J. Lasue, G. Lopez, J.M. Madariaga, L. Mandon, N. Mangold, P.Y. Meslin, A.E. Nelson, H. Newsom, A.L. Reyes-Newell, S. Robinson, F. Rull, S. Sharma, J.I. Simon, P. Sobron, I.T. Fernandez, A. Udry, D. Venhaus, S.M. McLennan, R. Morris, B. Ehlmann, Post-landing major element quantification using SuperCam laser induced breakdown spectroscopy, Spectrochim. Acta Part B: At. Spectrosc. (2022) 106347, http://dx.doi.org/10.1016/j.sab.2021.106347.

[29] S. Maurice, S.M. Clegg, R.C. Wiens, O. Gasnault, W. Rapin, O. Forni, A. Cousin, V. Sautter, N. Mangold, L. Le Deit, M. Nachon, R.B. Anderson, N.L. Lanza, C. Fabre, V. Payre, J. Lasue, P.Y. Meslin, R.J. Leveille, B.L. Barraclough, P. Beck, S.C. Bender, G. Berger, J.C. Bridges, N.T. Bridges, G. Dromart, M.D. Dyar, R. Francis, J. Frydenvang, B. Gondet, B. Ehlmann, K.E. Herkenhoff, J.R. Johnson, Y. Langevin, M.B. Madsen, N. Melikechi, J.L. Lacour, S. Le Mouelic, E. Lewin, H.E. Newsom, A.M. Ollila, P. Pinet, S. Schroeder, J.B. Sirven, R.L. Tokar, M.J. Toplis, C. d'Uston, D.T. Vaniman, A.R. Vasavada, ChemCam activities and discoveries during the nominal mission of the Mars science laboratory in Gale crater, Mars, J. Anal. At. Spectrom. 31 (4) (2016) 863–889, http://dx.doi.org/10.1039/C5JA00417A.

[30] P.R. Mahaffy, C.R. Webster, S.K. Atreya, H. Franz, M. Wong, P.G. Conrad, D. Harpold, J.J. Jones, L.A. Leshin, H. Manning, T. Owen, R.O. Pepin, S. Squyres, M. Trainer, MSL Science Team, O. Kemppinen, N. Bridges, J.R. Johnson, M. Minitti, D. Cremers, J.F. Bell, L. Edgar, J. Farmer, A. Godber, M. Wadhwa, D. Wellington, I. McEwan, C. Newman, M. Richardson, A. Charpentier, L. Peret, P. King, J. Blank, G. Weigle, M. Schmidt, S. Li, R. Milliken, K. Robertson, V. Sun, M. Baker, C. Edwards, B. Ehlmann, K. Farley, J. Griffes, J. Grotzinger, H. Miller, M. Newcombe, C. Pilorget, M. Rice, K. Siebach, K. Stack, E. Stolper, C. Brunet, V. Hipkin, R. Léveillé, G. Marchand, P.S. Sánchez, L. Favot, G. Cody, A. Steele, L. Flückiger, D. Lees, A. Nefian, M. Martin, M. Gailhanou, F. Westall, G. Israël, C. Agard, J. Baroukh, C. Donny, A. Gaboriaud, P. Guillemot, V. Lafaille, E. Lorigny, A. Paillet, R. Pérez, M. Saccoccio, C. Yana, C. Armiens-Aparicio, J.C. Rodríguez, I.C. Blázquez, F.G. Gómez, J. Gómez-Elvira, S. Hettrich, A.L. Malvitte, M.M. Jiménez, J. Martínez-Frías, J. Martín-Soler, F.J. Martín-Torres, A.M. Jurado, L. Mora-Sotomayor, G.M. Caro, S.N. López, V. Peinado-González, J. Pla-García, J.A.R. Manfredi, J.J. Romeral-Planelló, S.A.S. Fuentes, E.S. Martinez, J.T. Redondo, R. Urqui-O'Callaghan, M.-P.Z. Mier, S. Chipera, J.-L. Lacour, P. Mauchien, J.-B. Sirven, A. Fairén, A. Hayes, J. Joseph, R. Sullivan, P. Thomas, A. Dupont, A. Lundberg, N. Melikechi, A. Mezzacappa, J. DeMarines, D. Grinspoon, G. Reitz, B. Prats, E. Atlaskin, M. Genzer, A.-M. Harri, H. Haukka, H. Kahanpää, J. Kauhanen, O. Kemppinen, M. Paton, J. Polkko, W. Schmidt, T. Siili, C. Fabre, J. Wray, M.B. Wilhelm, F. Poitrasson, K. Patel, S. Gorevan, S. Indyk, G. Paulsen, S. Gupta, D. Bish, J. Schieber, B. Gondet, Y. Langevin, C. Geffroy, D. Baratoux, G. Berger, A. Cros, C. d'Uston, O. Forni, O. Gasnault, J. Lasue, Q.-M. Lee, S. Maurice, P.-Y. Meslin, E. Pallier, Y. Parot, P. Pinet, S. Schröder, M. Toplis, E. Lewin, W. Brunner, E. Heydari, C. Achilles, D. Oehler, B. Sutter, M. Cabane, D. Coscia, G. Israël, C. Szopa, G. Dromart, F. Robert, V. Sautter, S.L. Mouélic, N. Mangold, M. Nachon, A. Buch, F. Stalport, P. Coll, P. François, F. Raulin, S. Teinturier, J. Cameron, S. Clegg, A. Cousin, D. DeLapp, R. Dingler, R.S. Jackson, S. Johnstone, N. Lanza, C. Little, T. Nelson, R.C. Wiens, R.B. Williams, A. Jones, L. Kirkland, A. Treiman, B. Baker, B. Cantor, M. Caplinger, S. Davis, B. Duston, K. Edgett, D. Fay, C. Hardgrove, D. Harker, P. Herrera, E. Jensen, M.R. Kennedy, G. Krezoski, D. Krysak, L. Lipkaman, M. Malin, E. McCartney, S. McNair, B. Nixon, L. Posiolova, M. Ravine, A. Salamon, L. Saper, K. Stoiber, K. Supulver, J. Van Beek, T. Van Beek, R. Zimdar, K.L. French, K. Iagnemma, K. Miller, R. Summons, F. Goesmann, W. Goetz, S. Hviid, M. Johnson, M. Lefavor, E. Lyness, E. Breves, M.D. Dyar, C. Fassett, D.F. Blake, T. Bristow, D. DesMarais, L. Edwards, R. Haberle, T. Hoehler, J. Hollingsworth, M. Kahre, L. Keely, C. McKay, M.B. Wilhelm, L. Bleacher, W. Brinckerhoff, D. Choi, J.P. Dworkin, J. Eigenbrode, M. Floyd, C. Freissinet, J. Garvin, D. Glavin, A. Jones, D.K. Martin, A. McAdam, A. Pavlov, E. Raaen, M.D. Smith, J. Stern, F. Tan, M. Meyer, A. Posner, M. Voytek, R.C. Anderson, A. Aubrey, L.W. Beegle, A. Behar, D. Blaney, D. Brinza, F. Calef, L. Christensen, J.A. Crisp, L. DeFlores, B. Ehlmann, J. Feldman, S. Feldman, G. Flesch, J. Hurowitz, I. Jun, D. Keymeulen, J. Maki, M. Mischna, J.M. Morookian, T. Parker, B. Pavri, M. Schoppers, A. Sengstacken, J.J. Simmonds, N. Spanovich, M. de la Torre Juarez, A.R. Vasavada, A. Yen, P.D. Archer, F. Cucinotta, D. Ming, R.V. Morris, P. Niles, E. Rampe, T. Nolan, M. Fisk, L. Radziemski, B. Barraclough, S. Bender, D. Berman, E.N. Dobrea, R. Tokar, D. Vaniman, R.M.E. Williams, A. Yingst, K. Lewis, T. Cleghorn, W. Huntress, G. Manhès, J. Hudgins, T. Olson, N. Stewart, P. Sarrazin, J. Grant, E. Vicenzi, S.A. Wilson, M. Bullock, B. Ehresmann, V. Hamilton, D. Hassler, J. Peterson, S. Rafkin, C. Zeitlin, F. Fedosov, D. Golovin, N. Karpushkina, A. Kozyrev, M. Litvak, A. Malakhov, I. Mitrofanov, M. Mokrousov, S. Nikiforov, V. Prokhorov, A. Sanin, V. Tretyakov, A. Varenikov, A. Vostrukhin, R. Kuzmin, B. Clark, M. Wolff, S. McLennan, O. Botta, D. Drake, K. Bean, M. Lemmon, S.P. Schwenzer, R.B. Anderson, K. Herkenhoff, E.M. Lee, R. Sucharski, M.A. de Pablo Hernández, J.J.B. Ávalos, M. Ramos, M.-H. Kim, C. Malespin, I. Plante, J.-P. Muller, R. Navarro-González, R. Ewing, W. Boynton, R. Downs, M. Fitzgibbon, K. Harshman, S. Morrison, W. Dietrich, O. Kortmann, M. Palucis, D.Y. Sumner, A. Williams, G. Lugmair, M.A. Wilson, D. Rubin, B. Jakosky, T. Balic-Zunic, J. Frydenvang, J.K. Jensen, K. Kinch, A. Koefoed, M.B. Madsen, S.L.S. Stipp, N. Boyd, J.L. Campbell, R. Gellert, G. Perrett, I. Pradler, S. VanBommel, S. Jacob, S. Rowland, E. Atlaskin, H. Savijärvi, E. Boehm, S. Böttcher, S. Burmeister, J. Guo, J. Köhler, C.M. García, R. Mueller-Mellin, R. Wimmer-Schweingruber, J.C. Bridges, T. McConnochie, M. Benna, H. Bower, A. Brunner, H. Blau, T. Boucher, M. Carmosino, H. Elliott, D. Halleaux, N. Rennó, B. Elliott, J. Spray, L. Thompson, S. Gordon, H. Newsom, A. Ollila, J. Williams, P. Vasconcelos, J. Bentz, K. Nealson, R. Popa, L.C. Kah, J. Moersch, C. Tate, M. Day, G. Kocurek, B. Hallet, R. Sletten, R. Francis, E. McCullough, E. Cloutis, I.L. ten Kate, R. Kuzmin, R. Arvidson, A. Fraeman, D. Scholes, S. Slavney, T. Stein, J. Ward, J. Berger, J.E. Moores, Abundance and isotopic composition of gases in the martian atmosphere from the curiosity rover, Science 341 (6143) (2013) 263–266, http://dx.doi.org/10.1126/science.1237966.

[31] O. Gasnault, J. Mazoyer, A. Cousin, P.Y. Meslin, J. Lasue, J.L. Lacour, A. Ollila, G. Berger, O. Forni, S. Maurice, R.C. Wiens, S.M. Clegg, J.G. Blank, Deciphering sample and atmosphere oxygen contents with ChemCam on Mars, in: Lunar and Planetary Science Conference, 2012, p. 2888.

[32] P. Beck, O. Forni, J. Lasue, E. Lewin, A. Cousin, S. Maurice, P.Y. Meslin, W. Rapin, O. Gasnault, R. Wiens, N. Mangold, V. Sautter, P. Coll, C. Szopa, T. Dequaire, J. Blank, Carbon detection with ChemCam: laboratory studies and Mars results, in: Lunar and Planetary Science Conference, 2016, p. 1826.

[33] S. Schroeder, K. Rammelkamp, D. Vogt, O. Gasnault, H.W. Huebers, Contribution of a martian atmosphere to laser-induced breakdown spectroscopy (LIBS) data and testing its emission characteristics for normalization applications, Icarus 325 (2019) 1–15, http://dx.doi.org/10.1016/j.icarus.2019.02.017.

[34] A.M. Ollila, J.G. Blank, R.C. Wiens, J. Lasue, H.E. Newsom, S.M. Clegg, A. Cousin, S. Maurice, Preliminary results on the capabilities of the ChemCam lase-induced breakdown spectroscopy (LIBS) instrument to detect carbon on Mars, in: Lunar and Planetary Science Conference, 2011, p. 2395.

[35] A. Cousin, O. Forni, S. Maurice, O. Gasnault, C. Fabre, V. Sautter, R. Wiens, J. Mazoyer, Laser induced breakdown spectroscopy library for the Martian environment, Spectrochim. Acta Part B: At. Spectrosc. 66 (11–12) (2011) 805–814, http://dx.doi.org/10.1016/j.sab.2011.10.004.

[36] D.E. Anderson, B. Ehlmann, O. Forni, S.M. Clegg, A. Cousin, N.H. Thomas, J. Lasue, D.M. Delapp, R.E. McInroy, O. Gasnault, M.D. Dyar, S. Schroeder, S. Maurice, R. Wiens, Characterization of LIBS emission lines for the identification of chlorides, carbonates, and sulfates in salt/basalt mixtures for the application to MSL ChemCam data: LIBS OF CL, C, S IN SALT-BASALT MIXTURES, J. Geophys. Res.: Planets 122 (4) (2017) 744–770, http://dx.doi.org/10.1002/2016JE005164.

[37] C.R. Ytsma, M.D. Dyar, Accuracies of lithium, boron, carbon, and sulfur quantification in geological samples with laser-induced breakdown spectroscopy in Mars, Earth, and vacuum conditions, Spectrochim. Acta Part B: At. Spectrosc. 162 (2019) http://dx.doi.org/10.1016/j.sab.2019.105715.

[38] D. Vogt, S. Schroeder, S. Frohmann, P. Hansen, F. Seel, M. Gensch, H.W. Huebers, Spatiotemporal characterization of the laser-induced plasma plume in simulated Martian conditions, Spectrochim. Acta: Part A (2022) http://dx.doi.org/10.1016/j.sab.2021.106326.

[39] P. Beck, P.Y. Meslin, A. Fau, O. Forni, O. Gasnault, J. Lasue, A. Cousin, S. SChroeder, S. Maurice, R. Wiens, A. Ollila, E. Dehouck, N. Mangold, B. Garcia, S. Schwartz, W. Goetz, N. Lanza, Detectability of carbon 1 with ChemCam LIBS: distinguishing sample from mars atmospheric carbon, and application to Gale crater, Spectrochim. Acta Part B: At. Spectrosc. 408 (2024) http://dx.doi.org/10.1016/j.icarus.2023.115840.

[40] F. Chen, C. Sun, S. Qu, B. Zhang, Y. Rao, T. Sun, Y.Y. Sara Zhao, J. Yu, Determination of inorganic and organic carbons in a Martion soil simulant under the Martian CO2 atmospher using LIBS coupled with machine learning, Spectrochim. Acta Part B: At. Spectrosc. 214 (2024) http://dx.doi.org/10.1016/j.sab.2024.106887.

[41] D. Hahn, N. Omenetto, Laser-induced breakdown spectroscopy (LIBS), Part II: Review of instrumental and methodological approaches to material analysis and applications to different fields, Appl. Spectrosc. (2012) http://dx.doi.org/10.1366/11-06574.

[42] E. Monge, C. Aragon, J. Aguilera, Space- and time-resolved measurements of temperatures and electron densities of plasmas formed during laser ablation of metallic samples, Appl. Phys. A (1999) http://dx.doi.org/10.1007/s003399900297.

[43] J. Siegel, G. Epurescu, A. Perea, F. Gorillo-Vazquez, J. Gonzalo, C. Afonso, High spatial resolution in laser-induced breakdown spectroscopy of expanding plasmas, Spectrochim. Acta Part B: At. Spectrosc. (2005) http://dx.doi.org/10.1016/j.sab.2005.05.020.

[44] L. Mercadier, J. Hermann, C. Grisolia, A. Semerok, Diagnostics of nonuniform plasmas for elemental analysis via laser-induced breakdown spectroscopy: demonstration on carbon-based materials, J. Anal. At. Spectrom. (2013) http://dx.doi.org/10.1039/C3JA50127B.

[45] F. Seel, S. Schroeder, E. Clave, E. Dietz, P. Hansen, K. Rammelkamp, H.W. Huebers, Lifetime, size and emission of laser-induced plasmas for in-situ laser-induced breakdown spectroscopy on Earth, Mars and Moon, Icarus (2025) http://dx.doi.org/10.1016/j.icarus.2024.116376.

[46] A. De Giacomo, M. Dell'Aglio, R. Gaudiuso, G. Cristoforetti, S. Legnaioli, V. Palleschi, E. Tognoni, Spatial distribution of hydrogen and other emitters in aluminum laser-induced plasma in air and consequences on spatially integrated Laser-Induced Breakdown Spectroscopy measurements, Spectrochim. Acta Part B: At. Spectrosc. (2008) http://dx.doi.org/10.1016/j.sab.2008.06.010.

[47] F. Seel, Evolution of Plasmas and Shock Waves in Laser-Induced Breakdown Spectroscopy for Planetary Exploration (Ph.D. thesis), 2025.

[48] I. Gornuschkin, S. Shabanov, U. Panne, Abel inversion applied to a transient laser induced plasma: implications from plasma modeling, J. Anal. At. Spectrom. (2011) http://dx.doi.org/10.1039/C1JA10044K.

[49] A. Kramida, K. Olsin, Y. Ralchenko, J. Reader, R. Ibacache, E. Carpentier, T. Carpentier, A. Zimmerman, A. Hamins-Puertolas, M. Hamins-Puertolas, A. Sharova, G. Tan, E. Saloman, H. Kunari, J. Sansonetti, J. Fuhr, L. Podobedova, W. Wies, J. Curry, G. Dalton, R. Dragoset, F. Jou, W. Martin, P. Mohr, A. Musgrove, C. Sansonetti, G. Wiersma, Atomic Spectra Database, http://dx.doi.org/10.18434/T4W30F, URL: https://physics.nist.gov/PhysRefData/ASD/LIBS/libs-form.html.

[50] T. Smausz, B. Kondász, T. Gera, T. Ajtai, N. Utry, M. Pinter, G. Kiss-Albert, J. Budai, Z. Bozoki, G. Szabo, B. Hopp, Determination of UV–visible–NIR absorption coefficient of graphite bulk using direct and indirect methods, Appl. Phys. A 123 (10) (2017) 633, http://dx.doi.org/10.1007/s00339-017-1249-y.

[51] M. Brik, First-principles calculations of structural, electronic, optical and elastic properties of magnesite MgCO3 and calcite CaCO3, Phys. B 406 (4) (2011) 1004–1012, http://dx.doi.org/10.1016/j.physb.2010.12.049.

[52] J. Hermann, E. Axente, V. Craciun, A. Taleb, F. Pelascini, Evaluation of pressure in a plasma produced by laser ablation of steel, Spectrochim. Acta Part B: At. Spectrosc. 143 (2018) 63–70, http://dx.doi.org/10.1016/j.sab.2018.02.015.

[53] K.H. Williford, K.A. Farley, B.H. Horgan, B. Garczynski, A.H. Treiman, S. Gupta, A.J. Jones, S. Siljestroem, E. Clave, L. Mayhew, J.T. Osterhout, E. Ravanis, K.M. Stack, S. Fagents, C.C. Bedford, T. Bosak, S.V. Bykov, D. Flannery, K.P. Hand, M.W.M. Jones, L. Kah, A. Klidaras, J. Maki, L. Mandon, E. Mansbach, F.M. McCubbin, J.I. Simon, A. Srivastava, K. Uckert, R.C. Wiens, S. Alwmark, J. Aramendia, R. Barnes, P. Beck, J.F. Bell, S. Bernard, R. Bhartia, M.S. Bramble, A.J. Brown, A. Broz, D. Buckner, D.C. Catling, E. Cloutis, S. Connell, A. Corpolongo, A.D. Czaja, E. Dehouck, T. Fornaro, O. Forni, N.C. Haney, K. Hickman-Lewis, W. Hug, A. Koeppel, J.M. Madariaga, J. Martínez-Frías, J.I. Núñez, B.J. Orenstein, Y.Y. Phua, C. Pilorget, N. Randazzo, C. Royer, E.L. Scheller, N. Schmitz, S. Schroeder, M.A. Sephton, S. Sharma, S. Sharma, D. Shuster, K.P. Sinclair, A. Steele, C. Tate, B. Weiss, A.J. Williams, Z.U. Wolf, R.A. Yingst, Carbonated ultramafic igneous rocks in Jezero crater, Mars, Science (2025) eadu8264, http://dx.doi.org/10.1126/science.adu8264.

[54] S. Schroeder, E. Clave, P. Hansen, K. Rammelkamp, F. Seel, H.W. Huebers, A. Cousin, O. Forni, O. Gasnault, P. Pilleri, E. Dehouck, P. Beck, O. Beyssac, G. Foëx, T. Gabriel, S. Maurice, R. Wiens, Minor and trace element enhancements identified in SuperCam LIBS data with Spectral Unmixing, in: 55th Lunar and Planetary Science Conference, 2024.